



# Numerical Investigation on the Dielectric Working Fluid Effect on the Flow and Thermal Parameters of an Electrohydrodynamic Flat Heat Pipe

Open  
Access

Imène Saad<sup>1</sup>, Sameh Maalej<sup>1</sup>, Mohamed Chaker Zaghdoudi<sup>1,\*</sup>

<sup>1</sup> Laboratoire Matériaux, Mesures et Applications (MMA), Institut National des Sciences Appliquées et de Technologie (INSAT), University of Carthage, Centre Urbain Nord, BP N° 676 – 1080 Tunis Cédex, Tunisia

## ARTICLE INFO

## ABSTRACT

### Article history:

Received 23 December 2020

Received in revised form 12 October 2020

Accepted 14 October 2020

Available online 31 December 2020

The present work highlights the impact of the working dielectric fluid on the flow and the thermal parameters of an axially grooved flat mini heat pipe (FMHP) submitted to Electrohydrodynamic (EHD) effects. Three dielectric working fluids are considered: pentane, R123, and R141b. A model is developed by considering the Laplace-Young, mass, momentum, and energy balance equations. The numerical results show that the electric field affects the liquid distribution along the heat pipe and helps the condensate to flow back to the evaporator section. Moreover, under the electric field conditions, the vapor pressure drop increases, however, the liquid pressure drop decreases. The effect of the electric field on the liquid velocity depends on the FMHP zone, and the vapor velocity is hardly affected by the EHD effects. Furthermore, lower capillary driving pressures are required to provide the necessary capillary pumping under EHD conditions. Besides, pentane allows for higher vapor pressure drops compared to those obtained with R123 and R141b, while the liquid pressure drops are highest for R123. It is found that with R123, the liquid velocity is higher than that reached with R141b and pentane. It is also demonstrated that the capillary limit increases under EHD conditions, and for R141b, the capillary limit is the highest either in zero-field and EHD conditions. Best heat pipe thermal performances are observed for wide and deep grooves with R141b. Finally, the optimum fill charge allowing the maximum heat transfer capacity is determined for each working fluid and different groove dimensions. It is shown that the optimum fill charge is hardly affected by the electric field whatever the working fluid. R123 requires the highest optimum fill charge, however, the heat transport capacity of the FMHP is the lowest when using this working fluid.

### Keywords:

Electric field; heat pipe; grooves; working fluid; flow parameters; thermal parameters; maximum capillary limit; optimum fill charge

Copyright © 2021 PENERBIT AKADEMIA BARU - All rights reserved

## 1. Introduction

\* Corresponding author.

E-mail address: [chaker.zaghdoudi@insat.rnu.tn](mailto:chaker.zaghdoudi@insat.rnu.tn)

<https://doi.org/10.37934/arfmts.79.1.128152>

The use of heat pipes has become a common solution for electronics cooling applications. Their major advantages lie in their ability to transfer high heat fluxes under small temperature gradient, flexibility, high reliability, and their large heat capacity transport. The heat pipe operation is based on evaporation-condensation phenomena. Indeed, in contact with the heat source, the liquid is evaporated by absorbing heat at the evaporator, and the vapor, therefore, flows to the condenser where it releases the heat. The condensate flows back towards the evaporative region by capillary pumping which is ensured by the capillary structure (grooves, screen meshes, or sintered metal powder). The heat pipe thermal performances depend on the capillary structure, the heat sink temperature, the heat input power, and the environmental working conditions such as gravity and acceleration [1-2]. Besides, the proper operation of the heat pipe is based on the best choice of the capillary structure and the working fluid combination to provide the necessary capillary height.

For a capillary pumped heat pipe, the capillary merit number,  $M_c$ , which should be high in the range of the operating temperature, is used to assess the transport capacity of the working fluids according to Dunn and Reay [3].

$$M_c = \frac{\rho_l \cdot \sigma \cdot \Delta h_v}{\mu_l} \quad (1)$$

where  $\rho_l$ ,  $\sigma$ ,  $\Delta h_v$ , and  $\mu_l$  are the liquid density, the surface tension, the latent heat, and the liquid dynamic viscosity, respectively.

The capillary height can be estimated under no-flow conditions by Saad *et al.*, [4]

$$h_c = \frac{2\sigma \cdot \cos \alpha}{\rho_l \cdot g \cdot r_c} \quad (2)$$

where  $r_c$  is the effective capillary radius, and  $\alpha$  is the contact angle.

In flow conditions, the capillary pumping is ensured when the capillary driving pressure overcomes the vapor, the liquid, and the hydrostatic pressure drops according to

$$\Delta P_c \geq \Delta P_l + \Delta P_v + \Delta P_g \quad (3)$$

where  $\Delta P_c$ ,  $\Delta P_l$ ,  $\Delta P_v$ , and  $\Delta P_g$  are the driving capillary pressure, the pressure drops in the liquid and vapor phases, and the hydrostatic pressure drop, respectively.

An alternative technique to enhance the heat pipe thermal performance is the use of external fields such as magnetic or electric fields. The latter technique, the so-called electrohydrodynamic technique (EHD), is based on the interaction between an electric field and a working fluid. The physical principle of the electric field application in heat pipes is based on the fact that electric forces in the liquid-phase (condenser) are higher than that in the vapor phase (evaporator), which induces an EHD pumping of the condensate back to the evaporator. The electrical force per unit of volume that is responsible for the EHD flow is expressed by Durand [5]

$$\vec{f}_v = q_v \vec{E} - \frac{1}{2} E^2 \nabla \varepsilon + \frac{1}{2} \nabla \left( \rho \frac{d\varepsilon}{d\rho} E^2 \right) \quad (4)$$

$q_v$  is the volume density of the electrical charges,  $E$  is the electric field strength,  $\varepsilon$  and  $\rho$  are the fluid permittivity and the fluid density, respectively.

The first term of Eq. (4) represents the Coulomb force which acts on the electrical free charges. The second term represents the dielectrophoretic force generated by the spatial variations of the

dielectric permittivity of the fluid. Physically, this term represents the force exerted on the polarization charges that appear within the fluid under the action of an electric field. The third term of Eq. (4) is the electrostrictive force. It is due, on one hand, to the variations of the dielectric permittivity with the fluid density, on the other hand, to the non-uniformity of the electric field in the dielectric medium. The fluids that are used in combination with the EHD technique are dielectric ones that have low electrical conductivity. Hence, the electrical current intensity is very low leading to low electrical consumption.

For an EHD heat pipe, an EHD merit factor,  $M_{EHD}$ , which is similar to the capillary merit,  $M_c$ , has been identified and it is expressed by Jones [6]

$$M_{EHD} = \frac{(\epsilon_l - \epsilon_v) E_b^2 \rho_l \Delta h_v}{\mu_l} \quad (5)$$

where  $E_b$  is the breakdown electric field strength of the saturated vapor.  $\epsilon_l$  and  $\epsilon_v$  are the dielectric constants of the liquid and the vapor, respectively.

In the EHD Merit number, the term  $(\epsilon_l - \epsilon_v) E_b^2$  replaces the surface tension in the capillary Merit number; however, it depends on the breakdown field strength of the saturated vapor, which is not an intrinsic property of the fluid.

Under no-flow conditions, an electrical pumping height can be defined similarly to the capillary pumping height according to Jones [6]

$$h_{EHD} = \frac{(\epsilon_l - \epsilon_v) E^2}{2\rho_l g} \quad (6)$$

The EHD heat pipe works properly if the driving pressure provided by the combination of the EHD and the capillary forces is greater than the sum of all the pressure drops i.e. the pressure losses in the liquid and vapor phases and the hydrostatic pressure. This can be expressed by

$$\Delta P_{EHD} + \Delta P_c \geq \Delta P_l + \Delta P_v + \Delta P_g \quad (7)$$

where  $\Delta P_{EHD}$  is the EHD driving pressure.

Several experimental and theoretical studies dealing with the application of the EHD effects in heat pipes were carried out. They can be classified according to studies dealing with cylindrical heat pipes [6-17], and those dealing with flat heat pipes [18-28]. The choice of the working fluid affects strongly the EHD heat pipe operation. The most used dielectric fluids in heat pipes are pentane [17-21], R11 [7, 10, 11, 19], R113 [12, 13, 15, 16], R141b [17], and R123 [20].

Experimental works indicated that several advantages can be obtained by using electric fields in heat pipes among them we can distinguish: (1) the strong ability of the electric field to push the liquid from the condenser to the evaporator, (2) the significant enhancement of the heat transfer capacity rate and the active control of the temperature, and (3) the reduction or the elimination of the dry-out and the flooding zones.

Theoretical models have been improved and several numerical models available in the literature try to explain the EHD effects in axially grooved flat heat pipes. Suman [23] presented a theoretical study to analyze the EHD effects on a heat pipe including a grooved capillary structure with a triangular section. The results indicate that increasing the intensity of the electric field promotes the reduction of the dry-out length and allows to increase of the maximum heat transfer capacity due to the Coulomb forces contribution rather than the dielectrophoretic forces. Chang and Hung [24] studied the EHD effect on the operation of a flat heat pipe including a grooved capillary structure

composed of square-shaped microchannels. The results showed that the application of a non-uniform electric field promotes the condensate flow back to the evaporator and intensifies the capillary limit. Saad *et al.*, [25-27] studied the fluid flow and heat transfer in an EHD axially grooved flat heat pipe including square, triangular, and rectangular grooves. It was demonstrated that the higher is the electric field intensity, the lower is the capillary pumping required for the liquid flow [25]. Besides, higher electric field strengths were needed for the triangle grooves to observe similar effects to those observed for the square ones [26]. It was demonstrated that there is an optimum fill charge for which the power transferred by the heat pipe is maximum [27]. The effect of the electric field on the maximum heat input power is low for shallow grooves, whereas the maximum heat input power increases significantly for deep grooves [27].

The previous studies focused on the effects of the electric field strength [23, 25-26], the electrode configurations [24-25], and the groove shape [26] on the flow parameters. To our knowledge, no studies were carried out to highlight the impact of the working fluid on the thermal performance of electrohydrodynamic axially grooved flat heat pipes. The present paper aims to highlight and assess the combined effect of the nature of the working fluid and the use of an electric field on the flow and thermal parameters in an axially grooved flat heat pipe. Besides, this study allows identifying the optimum fill charges that enable to obtain the maximum heat transport capacity for given groove dimensions.

The evaluation of the FMHP performances in the presence and the absence of an electric field requires an analysis of the flow parameters (capillary radius, capillary pressure, liquid and vapor pressures, and velocities in both phases) since they affect considerably the maximum powers transferred according to Eq. (3) and (7). Likewise, the analysis of the forces exerted in the two phases and on the liquid-vapor interface provides undeniable clarifications that could explain the effect of the electric field on the flow and heat transfer in an FMHP. Finally, as the performance of the FMHP depends also on the working fluid fill charges and the dimensions of the grooves, an analysis of these parameters is necessary. The paper is structured around these orientations.

## 2. Description of The Modeled EHD Axially Grooved Flat Heat Pipe and Mathematical Formulation

The flat heat pipe is composed of five axial square-shaped grooves (Figure 1). Vertical electrodes are considered to promote the EHD pumping as it is shown by the section (A-A) of Figure 1. The liquid flows back to the evaporator along the corners and the vapor flows in the center of the groove (Figure 2). The EHD pumping, which originates from the electric forces, is such that the liquid flows from the condenser to the evaporator. The FMHP considered in this study is 100 mm length. The lengths of the evaporator, adiabatic, and condenser zones are 20 mm, 35 mm, and 45 mm, respectively. The thermophysical properties of the working fluids are listed in Table 1 for the saturation temperature  $T_{\text{sat}} = 30 \text{ }^\circ\text{C}$ . They are determined by REFPROP Software (version 8.0) [28].

**Table 1**  
 Thermophysical and electrical properties of pentane, R123, and R141b

| Working Fluid | N-Pentane                         | R123                               | R141b                              |
|---------------|-----------------------------------|------------------------------------|------------------------------------|
| $\rho_l$      | 615 kg/m <sup>3</sup>             | 1451.4 kg/m <sup>3</sup>           | 1224.3 kg/m <sup>3</sup>           |
| $\rho_v$      | 2.5 kg/m <sup>3</sup>             | 6.9 kg/m <sup>3</sup>              | 4.5 kg/m <sup>3</sup>              |
| $\sigma$      | 15 × 10 <sup>-3</sup> N/m         | 14.614 × 10 <sup>-3</sup> N/m      | 17.598 × 10 <sup>-3</sup> N/m      |
| $\mu_l$       | 202 × 10 <sup>-6</sup> kg/(m.s)   | 394.95 × 10 <sup>-6</sup> kg/(m.s) | 386.50 × 10 <sup>-6</sup> kg/(m.s) |
| $\mu_v$       | 6.782 × 10 <sup>-6</sup> kg/(m.s) | 10.909 × 10 <sup>-6</sup> kg/(m.s) | 9.338 × 10 <sup>-6</sup> kg/(m.s)  |
| $\Delta h_v$  | 361.6 kJ/kg                       | 169.33 kJ/kg                       | 223.76 kJ/kg                       |
| $M_c$         | 1.23 × 10 <sup>10</sup>           | 9.09 × 10 <sup>9</sup>             | 1.25 × 10 <sup>10</sup>            |
| $P_{sat}$     | 82060 Pa                          | 108990 Pa                          | 93742 Pa                           |
| $\alpha$      | 20°                               | 20°                                | 20°                                |
| $\epsilon_l$  | 1.8 $\epsilon_0$                  | 4.49 $\epsilon_0$                  | 4.5 $\epsilon_0$                   |
| $\epsilon_v$  | $\epsilon_0$                      | $\epsilon_0$                       | $\epsilon_0$                       |
| $q_v$         | 10 <sup>-5</sup> C/m <sup>3</sup> | 10 <sup>-5</sup> C/m <sup>3</sup>  | 10 <sup>-5</sup> C/m <sup>3</sup>  |

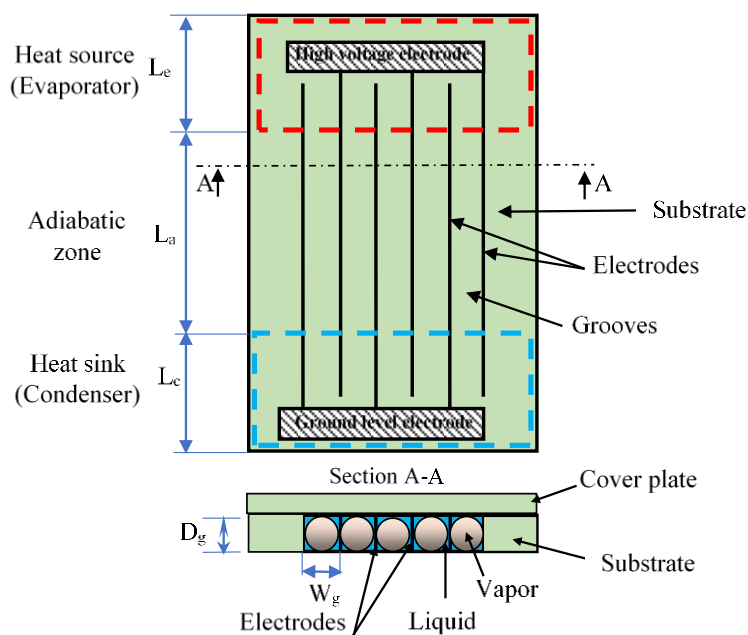


**Fig. 1.** Schematic of the EHD axially grooved flat heat pipe

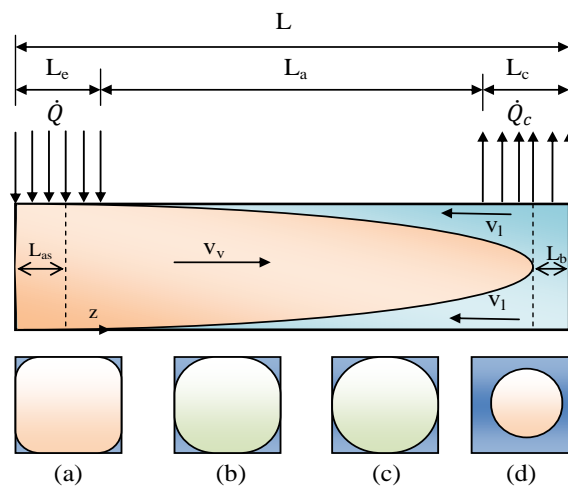


**Fig. 2.** Liquid-vapor flow evolution along one groove

The equations governing the electrohydrodynamically driven FMHP operation are developed by Saad *et al.*, [25-26], and summarized below

(i) The Laplace-Young equation which takes into account the electric forces that act on the liquid-vapor interface

$$\frac{dP_v}{dz} - \frac{dP_l}{dz} = -\frac{\sigma}{r_c^2} \frac{dr_c}{dz} + \frac{1}{2} (\epsilon_l - \epsilon_v) \frac{dE_0^2}{dz} \quad (8)$$

where  $P_v$  and  $P_l$  are the vapor and liquid pressures.  $r_c$  is the curvature radius of the liquid-vapor interface.  $E_0$  is the electric field strength.

(ii) The mass balance equations which are obtained by equalizing the mass flow rates entering and leaving an elementary volume of the liquid and vapor phases

$$\frac{d\dot{m}_l}{dz} = \frac{d(\rho_l A_l v_l)}{dz} = \frac{d\dot{m}_{il}}{dz} = \rho_l v_{il}(z) p_i \quad (9)$$

$$\frac{d\dot{m}_v}{dz} = \frac{d(\rho_v A_v v_v)}{dz} = \frac{d\dot{m}_{iv}}{dz} = -\rho_v v_{iv}(z) p_i \quad (10)$$

$$\frac{d\dot{m}_{il}}{dz} = \rho_l v_{il}(z) p_i = \frac{d\dot{m}_{iv}}{dz} = \rho_v v_{iv}(z) p_i \quad (11)$$

where  $\dot{m}_l$  and  $\dot{m}_v$  are the mass flow rates of the liquid and vapor phases, respectively.  $\dot{m}_{il}$  is the mass flow rate of the liquid vaporized through the liquid-vapor interface, and  $\dot{m}_{iv}$  is the mass flow rate of the vapor.  $\rho_l$  and  $\rho_v$  are the liquid and vapor densities, respectively.  $p_i$  is the liquid-vapor interfacial perimeter.  $A_l$  and  $A_v$  are liquid and vapor cross-sections, respectively.  $v_l$  and  $v_v$  are the liquid and vapor axial velocities.  $v_{il}$  and  $v_{iv}$  are the interfacial velocities at the liquid and vapor sides, respectively.

(iii) The momentum balance equations in the liquid and vapor phases which are obtained by determining the forces acting on an elementary volume and considering the Euler theorem

$$\rho_l \frac{d(A_l v_l^2)}{dz} = -\frac{d(A_l P_l)}{dz} + p_i \tau_{il} + p_{lw} \tau_{lw} - \rho_l g A_l \sin \beta - q_v E_l A_l - \frac{1}{2} (\epsilon_l - \epsilon_v) E_l^2 p_i \quad (12)$$

$$\rho_v \frac{d(A_v v_v^2)}{dz} = -\frac{d(A_v P_v)}{dz} - p_i \tau_{iv} - p_{vw} \tau_{vw} - \rho_v g A_v \sin \beta - q_v E_v A_v - \frac{1}{2} (\epsilon_l - \epsilon_v) E_v^2 p_i \quad (13)$$

The liquid and vapor sections,  $A_l$  and  $A_v$  as well as the liquid-wall,  $A_{lw}$ , the vapor-wall,  $A_{vw}$ , and the interfacial sections,  $A_i$  depend on the liquid-vapor interface radius and the contact angle (Figure 3).  $\tau_{vw}$  and  $\tau_{lw}$  are the vapor-wall and the liquid-wall viscous stresses, respectively.  $\tau_i$  is the liquid-vapor interfacial shear stress.  $p_{lw}$  and  $p_{vw}$  are the liquid-wall and vapor-wall perimeters, respectively. The expressions of these parameters are detailed in Saad *et al.*, [25-26].  $q_v$  is the volume density of the electrical charges.  $\epsilon_l$  and  $\epsilon_v$  are the liquid and vapor dielectric constants, respectively.  $E_l$  and  $E_v$  are the electric strength in the liquid and vapor phases, respectively.  $\beta$  is the inclination with respect to the horizontal. Hence,  $\beta = 0^\circ$  for the horizontal position,  $\beta = 90^\circ$  for the favorable vertical position (evaporator down and condenser up), and  $\beta = -90^\circ$  for the unfavorable vertical position (evaporator up and condenser down).

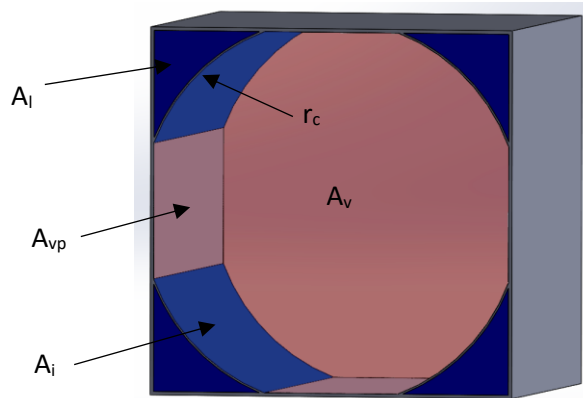


**Fig. 3.** Capillary radius and the different areas involved in the calculations

(iv) The energy balance equations for which the heat input power is supposed to contribute mainly to the phase change, and the thermal diffusion along the FMHP wall is neglected

$$\frac{dQ}{dz} = \frac{dm_l}{dz} \Delta h_v = \frac{d(\rho_l v_l A_l)}{dz} \Delta h_v \quad (14)$$

$$\frac{dQ}{dz} = -\frac{dm_v}{dz} \Delta h_v = -\frac{d(\rho_v v_v A_v)}{dz} \Delta h_v \quad (15)$$

$\Delta h_v$  is the latent heat and  $dQ/dz$  represents the variations of the heat flux rate in the evaporation, adiabatic, and condensation zones that are determined according to the following heat flux rate distribution

$$Q = \begin{cases} Q_a \frac{(z-L_{dr})}{(L_e-L_{dr})} & L_{dr} \leq z \leq L_e \\ Q_a & L_e < z < L_e + L_a \\ Q_a \left( \frac{L-(z-L_b)}{L_c-L_b} \right) & L_e + L_a \leq z \leq L - L_b \end{cases} \quad (16)$$

$L_e$ ,  $L_a$ , and  $L_c$  are the lengths of the evaporator, the adiabatic, and the condenser zones, respectively.  $L$  is the overall length of the FMHP, and  $L_b$  is the length of the blocked zone of the condenser which is flooded by the liquid (Figure 2(d)).  $L_{dr}$  is the length of the dried zone of the evaporator (Figure 2(a)).  $Q_a$  is the heat flux rate transferred axially along a microchannel of the FMHP. The dry-out length,  $L_{dr}$ , and the blocking length,  $L_b$ , are determined by performing the mass balance along the FMHP according to the following relation

$$M_0 = N_g \left[ \int_{L_{dr}}^{L-L_b} \rho_l A_l dz + \int_{L_{dr}}^{L-L_b} \rho_v A_v dz \right] + M_b \quad (17)$$

$N_g$  is the number of the grooves, and  $M_b$  is the blocking mass at the end of the condenser section which depends upon the operating conditions. The radius of curvature of the meniscus at the evaporator end cap,  $r_{cmin}$ , is found using Eq. (17).

The Laplace Young equation in Eq. (8) and the governing equations in Eq. (9)-(16) are resolved using the Runge-Kutta method of order 4 and a semi-implicit method is used. The computational procedure and numerical solving are described in Saad *et al.*, [25-26]. The following boundary conditions are considered

$$\begin{cases} r_c(z=0) = r_{cmin} \\ v_l(z=0) = v_v(z=0) = 0 \\ P_v(z=0) = P_{sat}(T_v) \\ P_l(z=0) = P_v - \frac{\sigma}{r_{cmin}} - \frac{1}{2}(\varepsilon_l - \varepsilon_v) E_0^2 \end{cases} \quad (18)$$

where  $T_v$  represents the saturated vapor temperature in the evaporator.

The solution is determined by an iterative process along the FMHP starting at the beginning of the evaporator ( $z = 0$ ) for which a radius of curvature  $r_c = r_{cmin}$  is initially selected. The minimum value of the radius of curvature is then determined to verify the principle of conservation of mass along the FMHP, but also to take into account the heat and mass transfer in the evaporator and condenser sections (Eq. (17)). The solving procedure is stopped when  $r_c = r_{cmax}$  by performing the following reasoning: the radius of curvature increases progressively from the evaporator towards the condenser. The attachment angle of the liquid film on the walls is assumed to be constant and equal to the contact angle (Figure 2(a) and 2(b)). When the contact points of the liquid film are joined, the vapor is no longer in contact with the wall and the structure of the vapor-liquid interface is as that shown in Figure 2(c). In this case, the radius of the curvature of the vapor-liquid interface is maximum ( $r_c = r_{cmax}$ ). Then gradually as the vapor condenses, the radius of curvature of the liquid-vapor interface decreases as the liquid film becomes thicker (Figure 2(d)). The maximum power transferred by the FMHP is such that corresponds to configuration of Figure 2(c). The position of this configuration is determined by performing mass balance along the FMHP. Thus, if the total mass that flows along the FMHP (term in the right of Eq. (17)) is greater than that introduced initially,  $M_o$ , it appears a dry-out zone at the evaporator and/or a flooding zone at the condenser and the lengths of these areas,  $L_{dr}$  and  $L_b$ , are determined.

### 3. Results and Discussion

#### 3.1 Model Validation

Up to now, no experimental studies dealing with the combined effects of the EHD and the working fluid on grooved FMHP operation have been published. Therefore, the validation of the results of our model is based on results that consider a flat grooved heat pipe operating in zero-field conditions and EHD conditions. Consequently, we have considered works that fit the model assumptions. Referring to Saad *et al.*, [25], the numerical results provided by our model are compared to the theoretical results obtained by Suman and Hoda [29] under zero-field conditions for a flat heat pipe including triangular grooves and the experimental results of Yu *et al.*, [22] for a flat heat pipe including rectangular grooves under EHD conditions. Both works consider pentane as a working fluid. The physical dimensions of the flat heat pipe and hydrodynamic parameters used in these investigations are summarized in Saad *et al.*, [25]. A good agreement is demonstrated between the results issued from the present model and those predicted by Suman and Hoda [29] and Yu *et al.*, [22].

#### 3.2 Flow Parameters Variations

##### 3.2.1 Capillary radius variations

The axial variations of the capillary radius i.e. the liquid-vapor radius of curvature for the three working fluids are depicted in Figure 4 under zero-field and EHD conditions for a heat input power of 0.3 W ( $W_g = D_g = 0.9$  mm) and a fill charge of 6 mg per groove. For these simulations, the FMHP is positioned horizontally ( $\beta = 0$ ). The radius of curvature increases along the heat pipe. Indeed, due to the evaporation phenomenon, the amount of the liquid is very low at the evaporator, which results

in a low value of the capillary radius. Since the condenser contains more liquid due to the condensation phenomenon, the liquid-vapor radius of curvature is greater than that in the evaporator. The liquid cross-section depends on the capillary radius. Thus, if the capillary radius is large, the grooves contain more liquid. Pentane allows for the highest liquid volume while for R123 the liquid volume is the lowest since the liquid density of pentane is the lowest and that of R123 is the highest, the filling mass being the same for the three working fluids. The electric field causes an increase of the capillary radius in the evaporator and adiabatic zones and its reduction in the condenser since the electric field promotes the return of the liquid from the condenser to the evaporator.

The variations of the relative gap between the capillary radii, which are obtained under EHD and zero-field conditions, are plotted as a function of the dimensionless length,  $z/L$ , for the different working fluids in Figure 5. The maximum increase in the capillary radius is 3 %, 5 %, and 21 % for pentane, R141b, and R123, respectively. It is reached at the beginning of the evaporator zone. Hence, the effect of the electric field on the liquid distribution is more pronounced for R123 and less marked for pentane. This can be explained by the fact that for R123, the grooves contain more vapor when compared to pentane and R141b. Indeed, in the case of R123, the grooves contain less liquid as it is mentioned previously. Moreover, R123 evaporates more easily as its latent heat is the lowest. Knowing that the electric field strength in the vapor phase is higher than that in the liquid phase due to the dielectric permittivity difference between the phases, the electric field strength in the grooves filled with R123 is higher than that in grooves filled with pentane and R141b. Hence, the application of an electric field is more effective for R123, especially in the evaporator section. We can also notice that the effect of the electric field on the capillary radius is almost the same for the three working fluids in an area located between the end of the adiabatic zone and the condenser end cap. This can be explained by the fact that the condenser section is filled with liquid and the electric field strength is almost the same for the three working fluids. Note that the maximum decrease of the curvature radius due to the electric field effect is reached in the condenser end cap. When compared to the capillary radius that is obtained under zero-field conditions, the maximum decrease of the capillary radius in EHD conditions is about 3 % for the three working fluids.

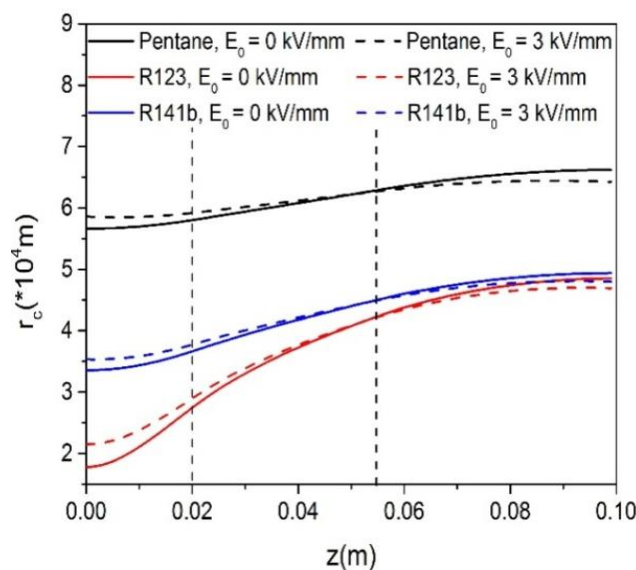


**Fig. 4.** Variations of the radius of curvature for pentane, R123, and R141b

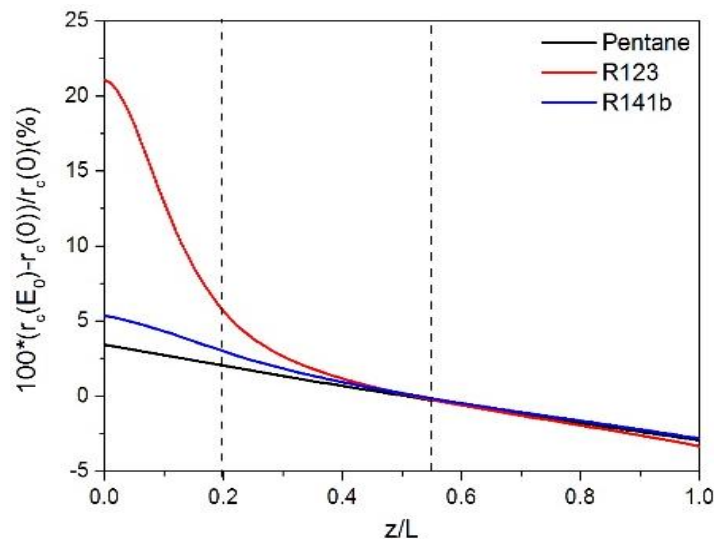
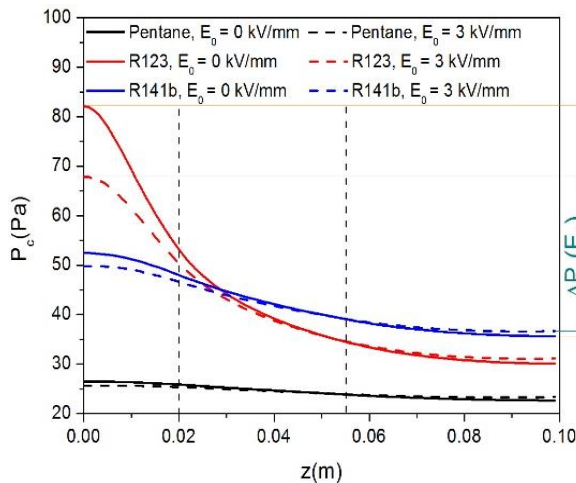


**Fig. 5.** Variations of the relative gap between  $r_c(E_0)$  and  $r_c(0)$  as a function of  $z/L$  for pentane, R123, and R141

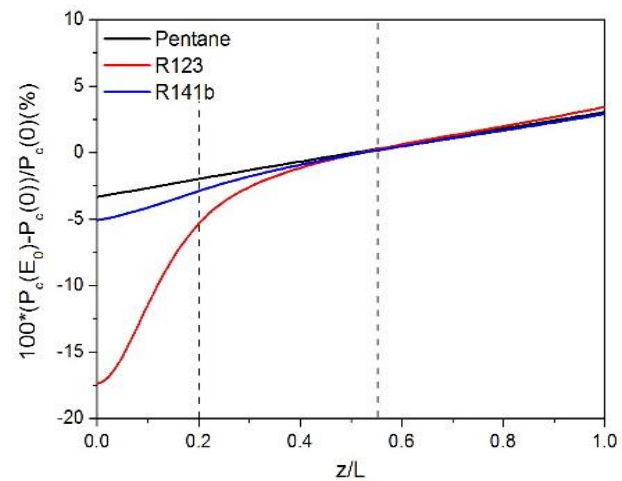
### 3.2.2 Capillary pressure variations

Figure 6 shows the variations of the capillary pressures ( $P_c = \sigma/r_c$ ). It decreases along the FMHP from the evaporator to the condenser since it is inversely proportional to the liquid-vapor radius of curvature. As shown, the lowest capillary pressures are reached with pentane for which the highest capillary radii are obtained. Moreover, the capillary pressure is reduced in the evaporation and adiabatic zones and augmented in the condensation zone when an electric field is applied. Hence, the electric field causes the reduction of the capillary driving pressure, which is the difference between the capillary pressures at the beginning of the evaporator and the end of the condenser section. Indeed, the capillary driving pressure decreases from 3.8 Pa ( $E_0 = 0$  kV/mm) to 2.2 Pa ( $E_0 = 3$  kV/mm), for pentane, and from 16.8 Pa ( $E_0 = 0$  kV/mm) to 13.1 ( $E_0 = 3$  kV/mm) for R141b, and from 52 Pa ( $E_0 = 0$  kV/mm) to 36.6 Pa ( $E_0 = 3$  kV/mm) for R123. The capillary driving pressure reduction is due to the EHD driving pressure that ensures the EHD pumping and reinforces the capillary pumping (Eq. (7)). Hence, the EHD driving pressures are 0.1 Pa, 0.5 Pa, and 4.1 Pa for pentane, R141b, and R123, respectively. This indicates that the highest EHD driving pressures are obtained with R123 because high electric strengths are achieved since grooves filled with R123 contain more vapor than the ones filled with pentane and R141b.

The variations of the relative gap between the capillary pressures that are obtained under EHD and zero-field conditions are depicted in Figure 7 as a function of the dimensionless length,  $z/L$ , for the different working fluids. The maximum decrease of the capillary pressure is reached at the beginning of the evaporator. It is 3 %, 5 %, and 17.5 % for pentane, R141b, and R123, respectively. The maximum increase of the capillary pressure due to the application of an electric field, which is reached at the condenser end, is nearly 2.5 % for the three working fluids.



**Fig. 6.** Axial variations of the capillary pressure for pentane, R123, and R141b



**Fig. 7.** Variations of the relative gap between  $P_c(E_0)$  and  $P_c(0)$  as a function of  $z/L$ , for pentane, R123, and R141b

### 3.2.3 Vapor pressure variations

The variations of the vapor pressure are illustrated in Figure 8. The vapor pressure decreases in the direction of the vapor flow that is from the evaporator to the condenser in zero-field and EHD conditions. The curves exhibit a smooth slope as they approach the condenser end cap. This is due to the attenuation of the vapor-wall and vapor-liquid friction since in the condenser, the vapor disappears in favor of the liquid as it will be demonstrated in sub-section 3.3.3. It should be noted that this will depend on the filling charge. Indeed, for optimum filling, the configuration of Figure 2(c) is obtained at the end of the condenser ( $L_b = 0$ : no blocking length i.e. no flooding zone). Under these conditions, both phases exist, and the vapor-liquid and vapor-wall frictions are still effective. For a fill charge that is greater than the optimum one, a blocking zone appears, and the curves exhibit smoother slopes as they approach the condenser end. Note that the calculations do not continue beyond this zone filled with liquid which does not participate in the flow.

The total vapor pressure drop is very low, and it is not exceeding 1 Pa for all the working fluids under zero-field conditions. Under EHD conditions, the total vapor pressure drop increases slightly. Thus, it passes from 0.5 Pa ( $E_0 = 0$  kV/mm) to nearly 1.2 Pa ( $E_0 = 3$  kV/mm) for pentane (Figure 8(a)), while it passes from 0.38 Pa ( $E_0 = 0$  kV/mm) to 0.79 Pa ( $E_0 = 3$  kV/mm) for R141b (Figure 8(c)) and increases from 0 Pa ( $E_0 = 0$  kV/mm) to 0.8 Pa ( $E_0 = 3$  kV/mm) for R123 (Figure 8(b)). The total pressure drop augmentation in the vapor phase is mainly due to the vapor velocity increase. Indeed, since the electric field contributes to the liquid flow back to the evaporator, the vapor cross-section flow is reduced along the evaporator and adiabatic zones according to the mass balance principle. Consequently, the vapor velocity increases in these zones causing augmentation of the vapor pressure drop. Under the same electric field conditions, using pentane allows for the highest vapor pressure drop since higher vapor velocities are reached with pentane as it will be demonstrated in sub-section 3.2.6.

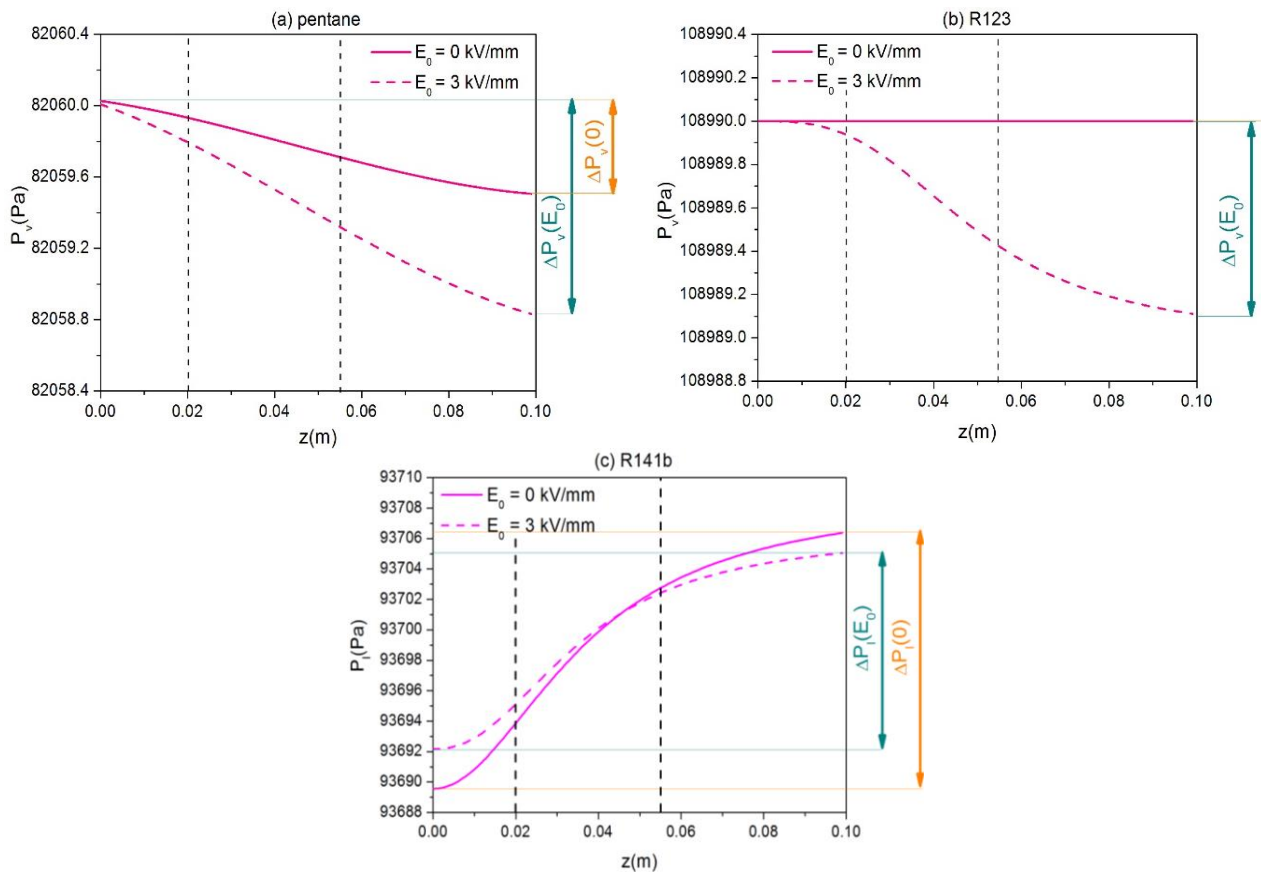


**Fig. 8.** Axial variations of the vapor pressure for (a) pentane, (b) R123, and (c) R141b

### 3.2.4 Liquid pressure variations

The variations of the liquid pressure are shown in Figure 9. The liquid pressure decreases from the condenser to the evaporator due to the liquid-wall viscous forces. The liquid pressure variations depend greatly on the liquid distribution along the FMHP. When the electric field is applied, the liquid is pushed towards the evaporator. Hence, the evaporator and adiabatic zones contain more liquid and consequently the liquid pressure rises in these regions; however, the liquid pressure drops in the condenser since it contains less liquid. The highest liquid pressure drop is obtained with R123 under zero-field and EHD conditions since higher liquid velocities are reached with this working fluid as it will be shown in sub-section 3.2.6.

The electric field causes a reduction of the liquid pressure drop passing from 3.4 Pa under zero-field conditions to nearly 1.1 Pa under EHD conditions for pentane (Figure 9(a)), whereas, it passes from 52 Pa to 39.9 Pa for R123 (Figure 9(b)), and from 16.4 Pa to 12.3 Pa for R141b (Figure 9(c)). The pressure drop in the liquid phase is mainly due to the liquid velocity decrease. Under the electric field action, the liquid cross-section flow is augmented in the evaporator and adiabatic zones, since the electric field promotes the return of the condensate from the condenser to the evaporator. Hence, the liquid velocity decreases in these regions, and consequently, the wall-liquid viscous forces are reduced.

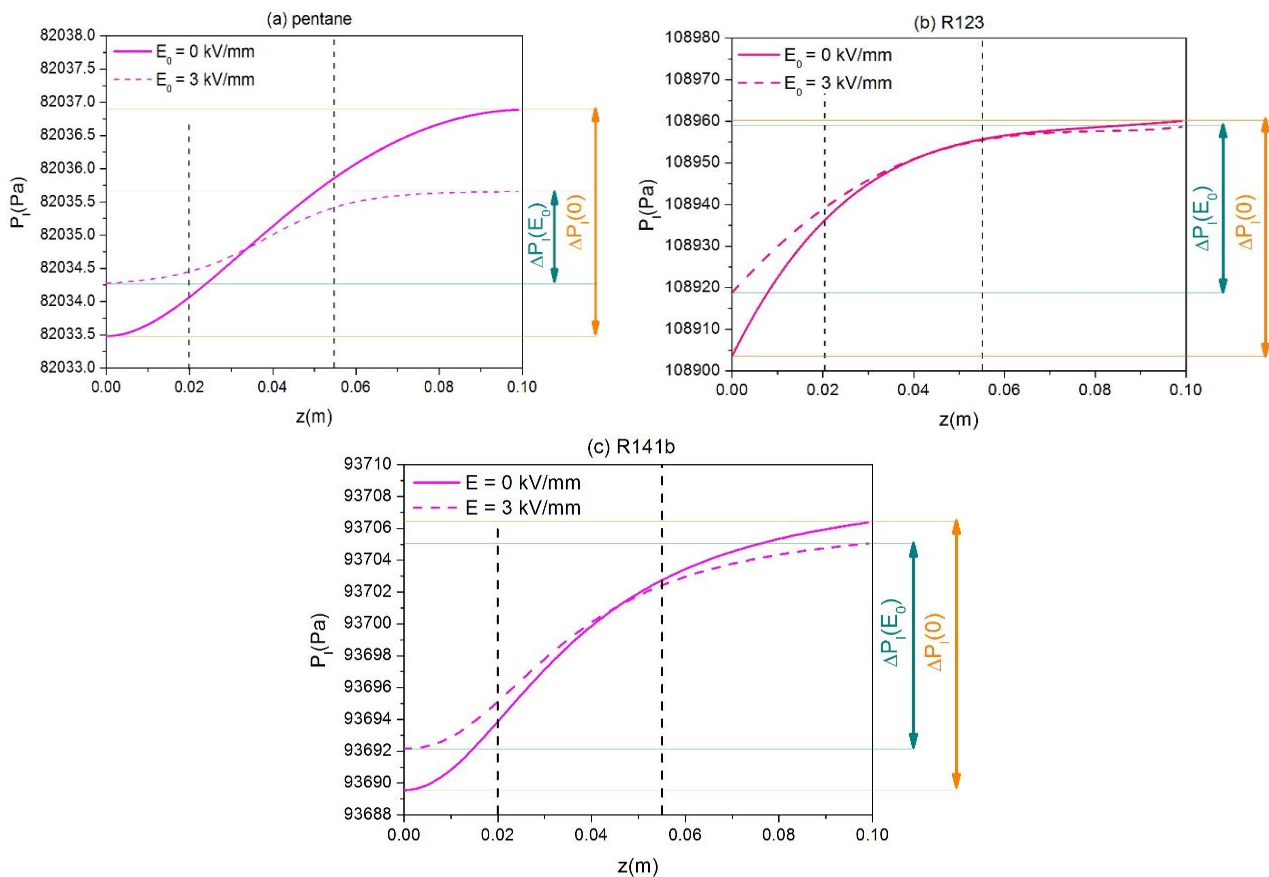


**Fig. 9.** Axial variations of the liquid pressure for (a) pentane (b) R123, and (c) R141b

### 3.2.5 Vapor velocity variations

The axial vapor velocity in the evaporator region increases sharply due to the active evaporation of the liquid, while it decreases in the condenser region and vanishes at its end (Figure 10). In the adiabatic section, as the vapor cross-section decreases, the vapor velocity increases. Pentane allows for the highest vapor velocities since low vapor cross-section is achieved with this working fluid. The electric field increases slightly the vapor velocity in the evaporator and adiabatic sections. The increase of the vapor velocity is not very significant under EHD conditions for the three working fluids as it is shown in Figure 11. The maximum increase in vapor velocity is obtained near the evaporator extremity. Hence, the maximum vapor velocity increase is about 1.5 % for R123 and R141b and about 2.5 % for pentane. The electric field hardly affects the vapor velocity in the condenser section for R123 and R141b. However, for pentane, the vapor velocity decreases by 1 % near the condenser end cap.

In the evaporator and a partial zone of the adiabatic section, the increase in the vapor velocity under the EHD conditions is mainly due to the reduction of the vapor cross-section since the electric field promotes the return of the liquid back to the evaporator. The decrease of the vapor velocity in the condenser section under the EHD conditions is due to the augmentation of the vapor cross-section as the liquid is pumped to the evaporator under the action of the electric field. For pentane, the vapor velocity rise is higher than that reached with R123 and R141b.

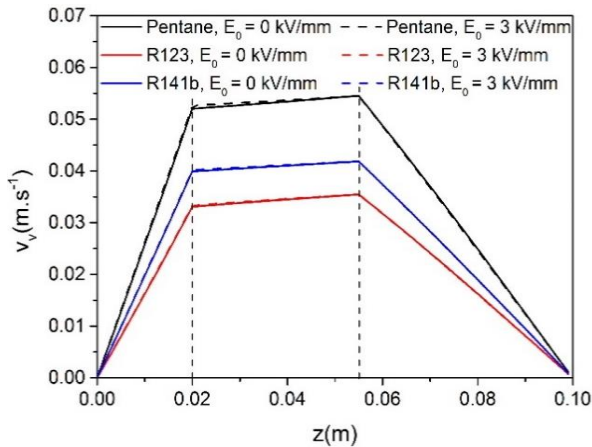


**Fig. 10.** Axial variations of the vapor velocity for pentane, R123, and R141b

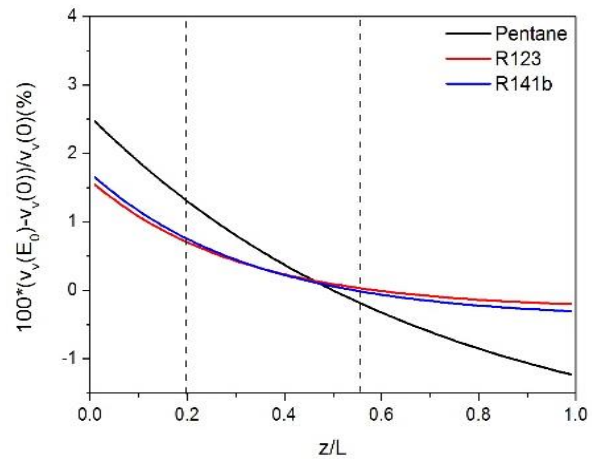


**Fig. 11.** Variations of the relative gap between  $v_v(E)$  and  $v_v(0)$  as a function of  $z/L$  for pentane, R123, and R141b

### 3.2.6 Liquid velocity variations

Figure 12 illustrates the evolutions of the axial liquid velocity along the grooves. The liquid velocity vanishes at the evaporator and condenser end cap (boundary conditions). In the evaporator, due to the evaporation phenomenon, the liquid cross-section decreases. As a result, the liquid velocity increases. In the adiabatic zone, the liquid cross-section rises, this causes a reduction of the liquid velocity. In the condenser, the liquid cross-section continues to grow due to the condensation phenomenon. Consequently, the liquid velocity decreases further. Additionally, it is observed that the liquid velocity value and profile depend on the working fluid. The highest liquid velocities are reached with R123 under zero-field conditions since the liquid cross-sections are the lowest for this working fluid as it is discussed in section 3.2.1 (Figure 4). Under EHD conditions, the liquid velocity is lower than that obtained in zero-field conditions in the evaporator and the adiabatic zones because the liquid-cross section grows in these zones since the electric field promotes the liquid flow back to the evaporator. The increase of the liquid velocity in the condenser is explained by the decrease of the liquid cross-section in this region under the effect of the electric field.

The variations of the relative gap between the liquid velocities obtained under EHD and zero-field conditions are shown in Figure 13 as a function of  $z/L$ , for the different working fluids. The maximum decrease in the liquid velocity, which is obtained near the evaporator extremity ( $z = 0$ ), is 6 %, 9.1 %, and 33 %, for pentane, R141b, and R123, respectively. It should be pointed out that, as for the capillary radius and the capillary pressure, the electric field has the same effect on the liquid velocity in the area located between the end of the adiabatic zone and the end of the condenser zone whatever the selected working fluid. Furthermore, under the EHD conditions, the liquid velocity is augmented in the condenser section and the maximum increase reaches nearly 10 %. The effect of the electric field on the liquid velocity decrease is more effective for R123. The significant decrease in the liquid velocity with R123 is attributed to the elevated vapor area in the grooves compared to that obtained with pentane and R141b. Hence, the electric field in the grooves filled with R123 is more intense than that in the grooves filled with R141b and pentane. Moreover, as the grooves are starved from liquid in the absence of an electric field as it is discussed in section 3.2.1, especially in the evaporator section, the EHD pumping ensures an effective liquid flow allowing to fill efficiently the grooves in the evaporator thus increasing the liquid cross-section, and consequently, reducing notably the liquid velocity. The effect of the electric field on the liquid velocity for the three working fluids is the same at the end of the adiabatic section and in the condenser because the electric field

strength is nearly the same for the three working fluids since the grooves are filled similarly with liquid in these locations.

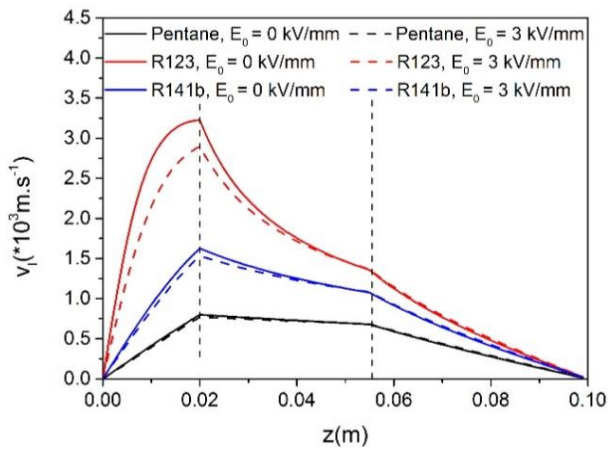


**Fig. 12.** Axial variations of the liquid velocity for pentane, R123, and R141b

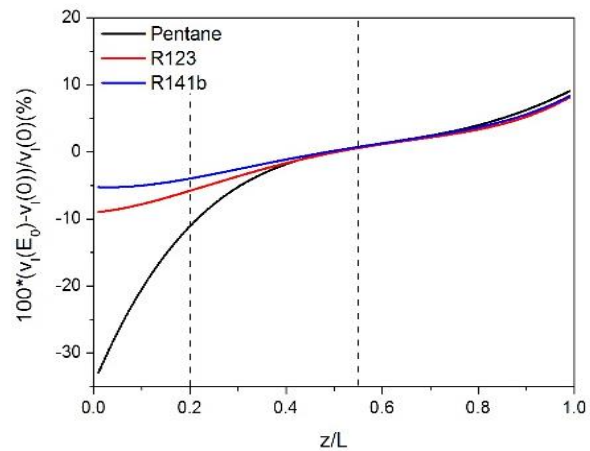


**Fig. 13.** Variations of the relative gap between  $v_l(E_0)$  and  $v_l(0)$  as a function of  $z/L$  for pentane, R123, and R141b

### 3.3 Variations of the Forces Along the FMHP

#### 3.3.1 Interfacial liquid-vapor shear forces

Figure 14(a) shows the axial evolutions of the liquid-vapor interfacial shear forces per unit of length. They are defined as the product of the interfacial shear stress,  $\tau_{il}$ , by the interfacial perimeter,  $p_i$ , and they depend on the vapor velocity but also the liquid-vapor radius of curvature [25-26]. Changes in interfacial forces are similar to those of the vapor velocity. They increase in the evaporation and adiabatic zones and decrease in the condensation zone. Moreover, under EHD conditions, the interfacial shear forces increase in the evaporator and the adiabatic zones. The maximum increase is reached at the evaporator end cap, and it is about 53 % for R123 and 15 % for pentane and R141b (Figure 14(b)). This can be explained by the vapor velocity and the liquid-vapor interfacial perimeter rise in these zones under the action of the electric field. However, in the condenser section, the liquid-vapor interfacial shear stresses decrease as the vapor velocity and the liquid-vapor perimeter are lowered in this region. The maximum reduction in the liquid-vapor interfacial forces, which is reached in the condenser end cap, is about 10 % for pentane and 5 % for R123 and R141b (Figure 14(b)). For pentane, the liquid-vapor interfacial shear forces are higher than those of R141b and R123 since for pentane, which allows for high liquid filling ratio, the vapor velocity, and the interfacial perimeter are greater than those obtained with R141b and R123.

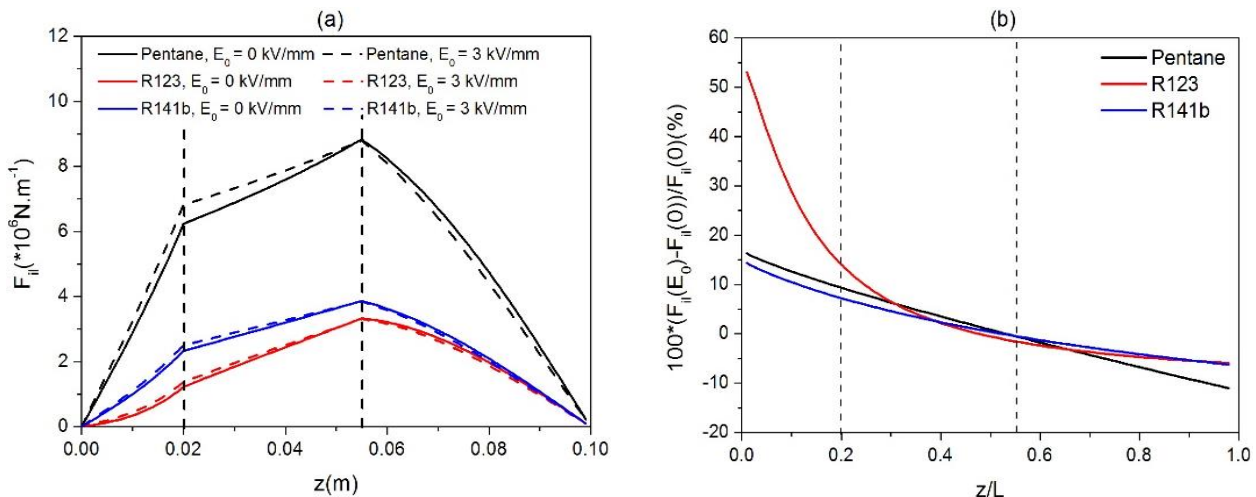


**Fig. 14.** Axial variations of (a) the interfacial liquid-vapor forces per unit of length,  $F_{ii}$ , and (b) the relative gap between  $F_{ii}(E_0)$  and  $F_{ii}(0)$ , for pentane, R123, and R141b

### 3.3.2 Liquid-wall viscous forces

The variations of the liquid-wall viscous forces per unit of length are depicted in Figure 15(a). They are calculated as the product of the liquid-wall viscous stress,  $\tau_{lw}$ , by the liquid-wall perimeter,  $p_{lw}$ . The obtained curve profiles are similar to those of the liquid velocity since the liquid-wall viscous forces are proportional to the liquid velocity [25-26]. The presence of an electric field reduces the liquid-wall viscous forces in the evaporator and adiabatic zones. The maximum reduction is reached at the evaporator end cap, and it is nearly 35 % for R123 and 9 % for pentane and R141b (Figure 15(b)). This result can be explained by the decrease of the liquid velocity even though the liquid-wall perimeter increases under the action of the electric field in these sections as the electric field promotes the return of the liquid back to the evaporator. In the condenser section, the liquid-wall viscous forces increase slightly in the presence of the electric field which has a little effect on the liquid velocity. The maximum rise in the liquid-wall viscous forces is the same for the three working fluids and it is about 5 % (Figure 15(b)). The highest liquid-wall viscous forces are obtained with R123, which allows for the highest liquid velocity in zero field and EHD conditions. Note that the electric field affects similarly the liquid-wall viscous forces for pentane and R141b.

The liquid-wall viscous forces are responsible for the liquid pressure drop. As it is indicated above, the liquid-wall forces decrease in two zones (evaporator and adiabatic zones) under EHD conditions and increase slightly in the condenser, so we can conclude that along the FHMP the liquid-wall forces decrease, and consequently, the liquid pressure drop is diminished. Note the liquid-wall forces are the highest for R123 which explains the highest value of the liquid pressure drop that is obtained with this working fluid under zero-field and EHD conditions.

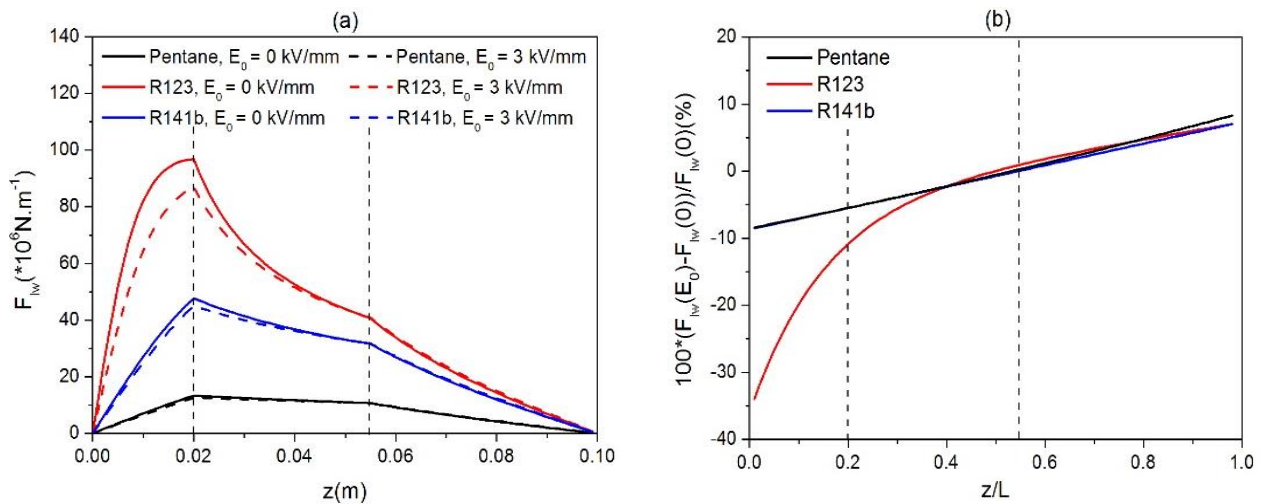


**Fig. 15.** Axial variations of (a) the liquid-wall viscous per unit of length,  $F_{lw}$ , and (b) the relative gap between  $F_{lw}(E_0)$  and  $F_{lw}(0)$ , for pentane, R123, and R141b

### 3.3.3 Vapor-wall viscous forces

The evolutions of the vapor-wall viscous forces per unit of length are plotted in Figure 16(a). They are defined as the product of the vapor-wall viscous stress,  $\tau_{vw}$ , by the vapor-wall perimeter,  $p_{vw}$ . This force depends on the vapor velocity and the capillary radius [25-26]. It increases in the evaporator and decreases in the adiabatic and condensation zones. Note that the variations of the vapor-wall forces are not similar to those of the vapor velocity in the adiabatic section since the vapor-wall decreases significantly in this region as the liquid is pumped back to the evaporator under the action of the electric field. The application of an electric field reduces the vapor-wall friction in the evaporator and adiabatic zones. The maximum reduction is reached at the evaporator end cap, and it is about 15 %, 8 %, and 5 % for pentane, R123, and R141b, respectively. However, in the condenser, the vapor-wall friction is augmented. The maximum augmentation is reached at the condenser end cap, and it is about 38 % for pentane and 5 % for R123 and R141b. The vapor-wall viscous forces are much lower than the liquid-wall viscous forces, but they have the same order of magnitude of the liquid-vapor shear forces. The highest vapor-wall viscous force is obtained with R123 and the lowest one is obtained with pentane. This is because the vapor-wall perimeter is the highest for R123 and the lowest for pentane.

The vapor-wall viscous forces and the liquid-vapor shear forces are responsible for the vapor pressure drop. As it is indicated above, under the action of an electric field, the vapor-wall forces decrease in two zones (evaporator and adiabatic zones) and increase in the condenser, however, as it is demonstrated in section 3.3.1, the liquid-vapor shear forces increase in the evaporator and adiabatic zones and decrease in the condenser under the action of the electric field. Hence, the combined effect of these two forces ( $F_{il} + F_{vw}$ ) is such that it increases along the FMHP whatever the section, and consequently, the vapor pressure drop is augmented when the electric field is applied. Note the sum of the vapor-wall forces and the liquid-vapor shear forces are highest for pentane which explains the highest value of the vapor pressure drop that is obtained with this working fluid under zero-field and EHD conditions.

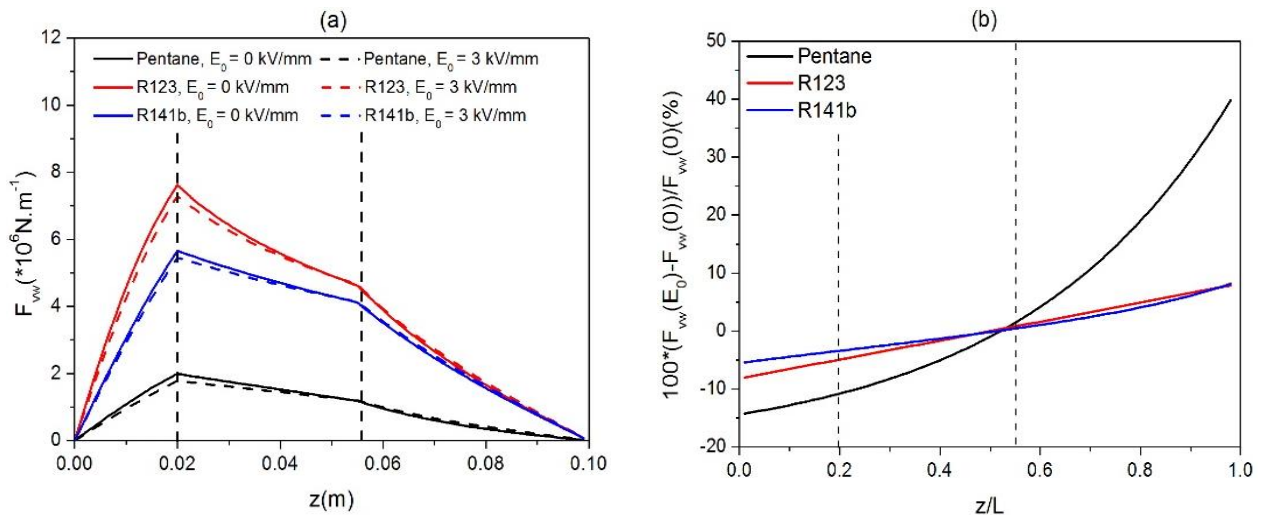


**Fig. 16.** Axial variations of (a) the vapor–wall viscous forces per unit of length,  $F_{vw}$ , and (b) the relative gap  $F_{vw}(E_0)$  and  $F_{vw}(0)$ , for pentane, R123, and R141b

### 3.3.4 Electrical forces

The variations of the electrical forces (Coulomb and dielectrophoretic forces) per unit of length are plotted in Figure 17, for the three working fluids. The Coulomb force in the liquid phase is calculated as the product of the electrical force volume density by the liquid area ( $F_{cl} = q_v E_l A_l$ ). The Coulomb force is reduced from the condenser to the evaporator indicating that this force tends to push the condensate towards the evaporator (Figure 17(a)). Besides, for R123, the Coulomb force exerted in the liquid phase is lowest and it is highest for pentane. This result is mainly attributed to the low liquid area that fills the grooves in the case of R123.

The variations of the Coulomb force in the vapor phase are plotted in Figure 17(b). It is defined as the product of the electrical force volume density by the vapor area ( $F_{cv} = q_v E_v A_v$ ). The Coulomb force exerted in the vapor phase has a reverse trend when compared to the Coulomb force in the liquid phase; hence, it decreases from the evaporator to the condenser. Moreover, the coulomb force in the vapor phase is much lower than that exerted in the liquid phase. The highest Coulomb force in the vapor phase is reached with R123 since this working fluid allows for a high vapor area.

Figure 17(c) illustrates the variations of the dielectric force per unit of length. It is calculated according to  $0.5 (\epsilon_l - \epsilon_v) E^2 p_i$ . The dielectric force has the same trend as the Coulomb force exerted in the liquid phase. Hence, it decreases from the condenser towards the evaporator indicating that it favors the condensate flow back. It is pointed out that the dielectric force is higher than the Coulomb forces. Although in the case of pentane, the liquid-vapor interfacial perimeter is the highest, nevertheless, this fluid has the lowest dielectric permittivity. Thus, for this working fluid, the dielectrophoretic forces are the weakest. R141b and R123 have similar dielectric constants, however, for R123, the liquid-vapor interfacial perimeter is lower than that for R141b. Thus, the dielectrophoretic forces in the case of R123 are lower than those in the case of R141b.

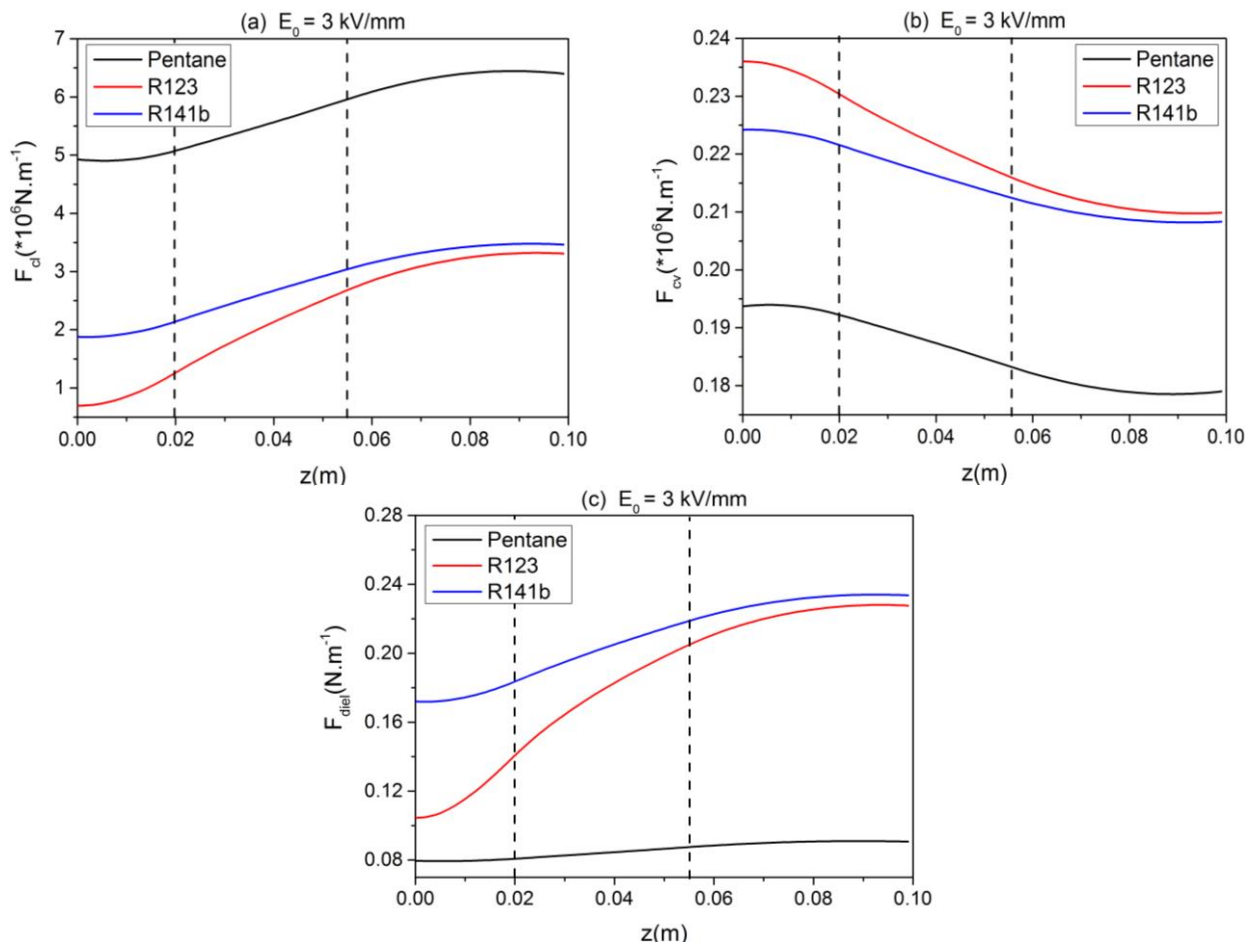


**Fig. 17.** Variations of the electrical forces per length unit for pentane, R123, and R141b: (a) the Coulomb force within the liquid phase, (b) the Coulomb force within the vapor phase, and (c) the dielectrophoretic force

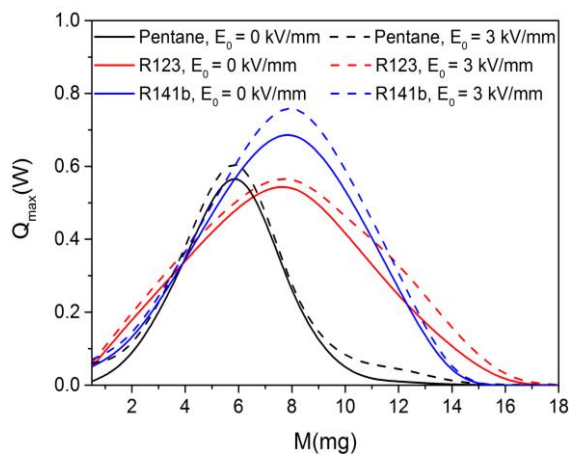
### 3.4 Variations of the Capillary Limit as A Function of the Fill Charge

Figure 18 shows the variations of the maximum heat transfer capacity,  $Q_{max}$ , as a function of the filling charge under zero-field and EHD conditions, for the different working fluids. Under zero-field conditions, the capillary limit occurs when the driving capillary pressure,  $\Delta P_c$ , balances the pressure drops in the liquid and vapor phases,  $\Delta P_l$  and  $\Delta P_v$ , as well as the hydrostatic pressure drop,  $\Delta P_g$ , (Eq. (3)). Under EHD conditions, the maximum heat transfer capillary is determined by balancing the capillary and the EHD driving pressures with the liquid, vapor, and hydrostatic pressure drops (Eq. (7)). The maximum heat transport capacity corresponds to a flow configuration such as no dry-out and flooding occur in the evaporator and condenser, respectively ( $L_{as} = L_b = 0$ ).

In these simulations, square grooves are considered ( $D_g = W_g = 0.8$  mm). Each of the obtained curves exhibits maxima corresponding to the optimum fill charge, for which the capillary limit of the FMHP, is maximum. Moreover, a filling charge, which is less than the optimum value, causes a reduction in the heat transfer capacity of the FMHP with a possibility of dry-out in the evaporator. Contrarily, a filling charge, which is greater than the optimum value, leads to an excess of liquid which remains blocked at the condenser, and reduces its effective length, thus causing a reduction in the capillary limit. Besides, maximum heat transport capacities are reached for R123 and R141b with nearly the same optimum fill charge, under zero-field and EHD conditions. For pentane, maximum heat transport capacities are reached for low optimum fill charges under the same conditions. Note

that the highest maximum heat transport capacity is achieved with R141b, however, R123 exhibits the lowest performance. To assess quantitatively the transport capacity of the different working fluids in the absence of an electric field, the merit number of each of the working fluid was calculated at an operating temperature of 30 °C as it is shown in Table 1. R141b exhibits the highest value of the Merit number, while R123 exhibits the smallest one. The Merit values explain the good thermal performances obtained with R141b for the operating temperature of 30 °C.

The maximum heat transport capacities that are reached under optimum fill charges under zero field and EHD conditions are reported in Figure 19. Under zero-field conditions, the maximum heat transfer capacities,  $Q_{max}$ , that are obtained with R123 and pentane are nearly the same (0.54 W for R123 and 0.56 W for pentane). However, for R141b,  $Q_{max} = 0.68$  W. When comparing the maximum heat transfer capacities obtained with pentane and R141b to that obtained with R123 under zero-field conditions, we can note that pentane and R141b allow for 3.7 % and 26 % enhancement, respectively (Figure 20(a)). The electric field allows for heat transport capacity enhancement for all the working fluids. Hence, an electric field intensity of 3 kV/mm allows for 3.7 %, 7.1 %, and 11 % enhancement for R123, pentane, and R141b, respectively (Figure 20(b)). Moreover, when referring to R123, the electric field ensures heat transfer capacity enhancement that reaches 7.1 % for pentane and 35 % for R141b, respectively (Figure 20 (c)).



**Fig. 18.** Variations of the maximum heat transport capacity as a function of the fill charge for the different working fluids ( $D_g = W_g = 0.8$  mm)

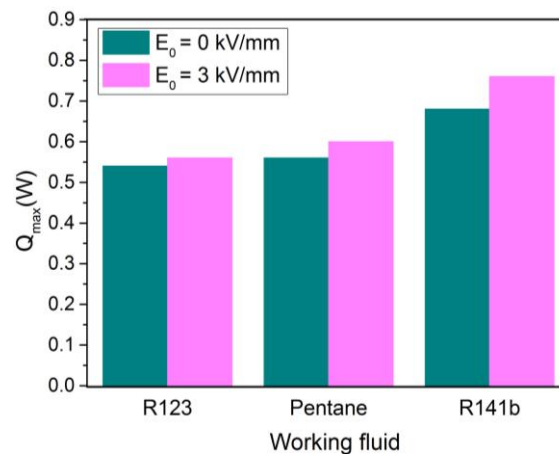


**Fig. 19.** Maximum heat transport capacities for optimum fill charges under zero-field and EHD conditions for the different working fluids ( $W_g = D_g = 0.8$  mm)

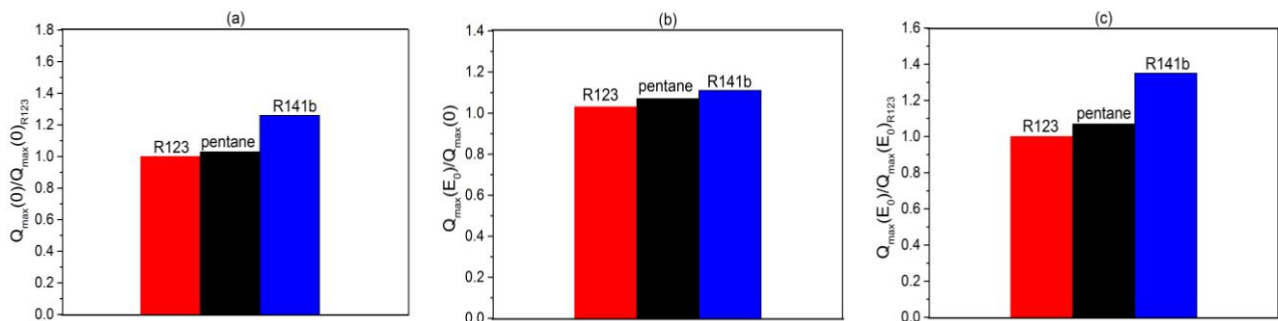


**Fig. 20.** Heat transport capacity enhancements under optimum fill charges when referring to: (a) R123 under zero-field conditions, (b) the zero-field conditions, and (c) R123 under EHD conditions ( $W_g = D_g = 0.8$  mm)

### 3.5 Variations of the Capillary Limit as A Function of the Groove Dimensions

The variations of  $Q_{max}$  as a function of the fill charge are shown in Figure 21 for pentane, R123, and R141b under zero-field and EHD conditions, for different groove dimensions. The optimum fill charge and the maximum transferred power,  $Q_{max}$ , increase with the groove dimensions. The best performances are obtained for large and deep grooves ( $1 \times 1 \text{ mm}^2$  cross-section). In Figure 22, are reported the maximum heat transport capacities for the different working fluids that are reached with optimum fill charges under zero-field and EHD conditions, for different groove dimensions. For narrow and shallow grooves ( $0.6 \times 0.6 \text{ mm}^2$  cross-section), all the working fluids allow for nearly the same heat transport capacity under zero-field and EHD conditions. For large and deep grooves, the heat transport capacity is the lowest for R123 under both zero-field and EHD conditions. However, R141b gives the best performances under both zero-field and EHD conditions.

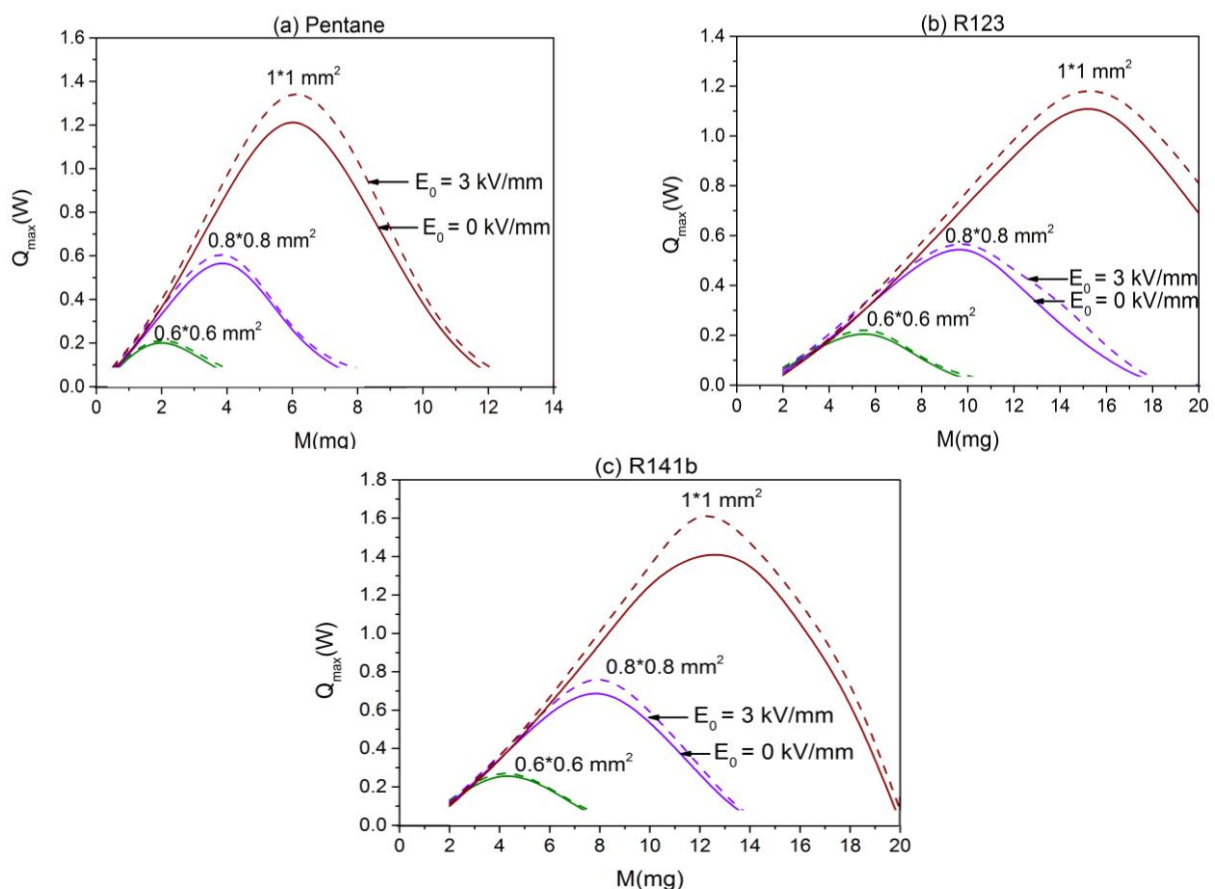


**Fig. 21.** Maximum heat transport capacities as a function of the fill charge for different groove dimensions and working fluids: (a) pentane, (b) R123, and (c) R141b

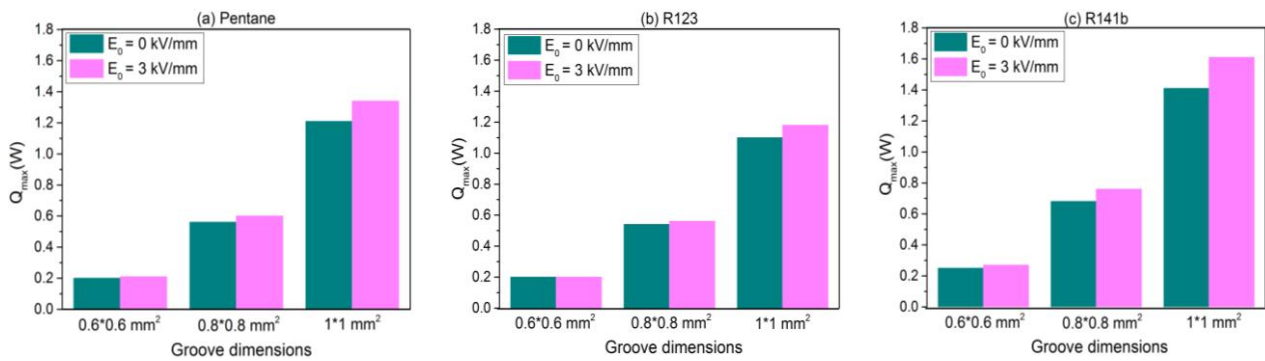


**Fig. 22.** Maximum heat transport capacity values for optimum fill charges under zero-field and EHD conditions for different groove dimensions: (a) pentane, (b) R123, and (c) R141b

Under zero-field conditions, when comparing the maximum heat transport capacity obtained with the different working fluids to that reached with R123 (Figure 23(a)), we can conclude that pentane and R141b allow for 3 % and 26 % enhancement, respectively, for narrow and shallow grooves; however, for large and deep grooves, pentane and R141b allow for nearly the same enhancement. Moreover, we can notice that the heat transport capacity increases significantly with pentane when operating with wide and deep grooves rather than narrow and shallow ones. For large and deep grooves, the heat transport capacity enhancement due to the application of an electric field differs from a working fluid to another. It is 7 %, 10 %, and 14 % for R123, pentane and R141b, respectively (Figure 23(b)). Finally, under EHD conditions, when comparing the maximum heat transport capacity attained with the different working fluids to that obtained with R123, we can notice that R141b allows for the highest maximum heat transport capacity enhancement passing from 22 % for narrow and shallow grooves to 36 % for wide and deep ones (Figure 23(c)).

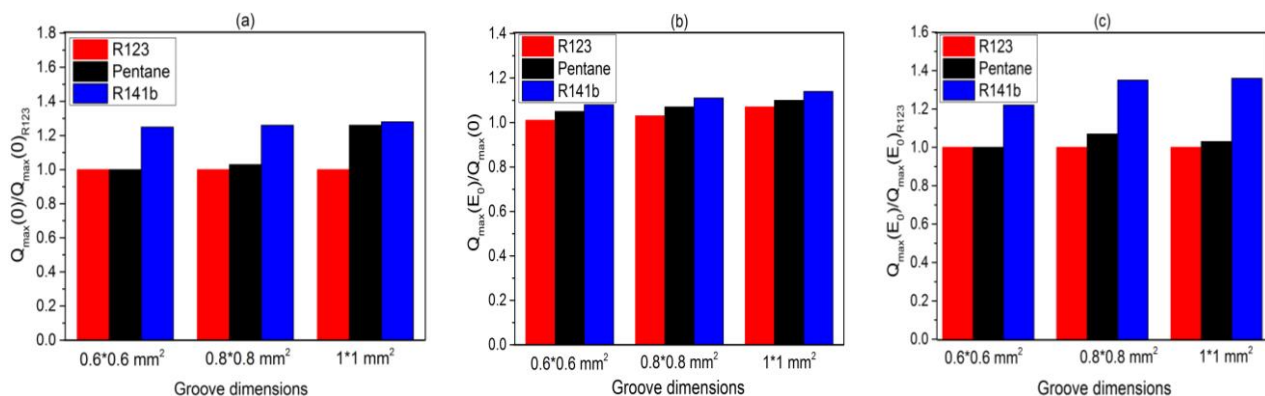


**Fig. 23.** Heat transport capacity enhancements under optimum fill charges when referring to (a) R123 under zero-field, (b) the zero-field conditions, and (c) R123 under EHD conditions, for different groove dimensions

The optimum fill charges are plotted in Figure 24 for the different working fluids under zero-field and EHD conditions. The optimum fill charge is hardly affected by the electric field whatever the working fluid and the groove dimensions. For R123, the optimum fill charge is the highest. The variations of the filling ratio as a function of the groove dimensions under zero-field and EHD conditions for the different working fluids are depicted in Figure 25. The filling ratio is defined as the ratio of the working fluid volume to the geometrical volume of the grooves. As for the optimum fill charge, the filling ratio is hardly affected by the action of the electric field whatever the working fluid. For pentane, the filling ratio increases slightly with the groove dimensions. For R123, the filling ratio variations as a function of the groove dimensions exhibit a minimum which is obtained for 0.8\*0.8

mm<sup>2</sup>; however, for R141b, the filling ratio variations exhibit a maximum which is obtained for the same groove dimensions.

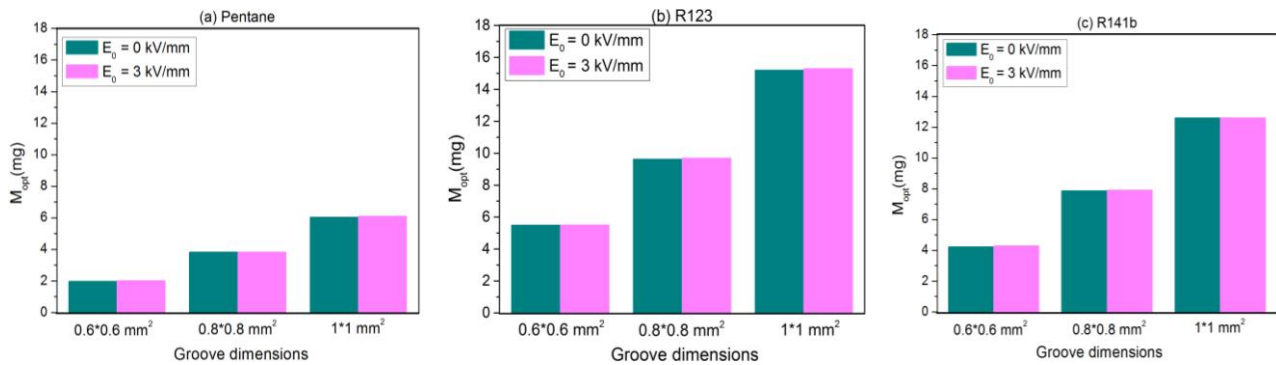


**Fig. 24.** Optimum fill charge as a function of the groove dimensions under zero-field and EHD conditions for the different working fluids: (a) pentane, (b) R123, and (c) R141b

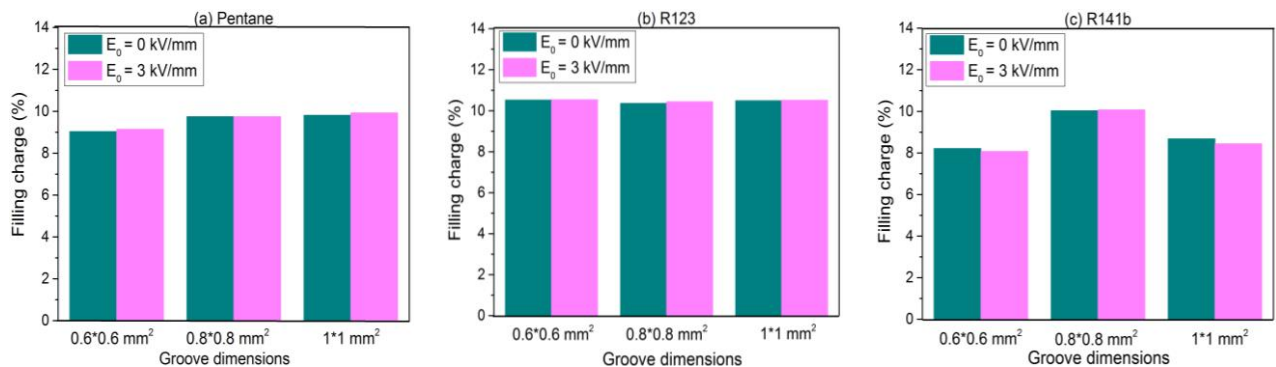


**Fig. 25.** Filling ratio as a function of the groove dimensions under zero-field and EHD conditions for the different working fluids: (a) pentane, (b) R123, and (c) R141b

#### 4. Conclusions

This paper reports on the investigation of the influence of the working fluid on the operation of an electrohydrodynamic FMHP including axial grooves. The following conclusions are drawn

- i. The electric field affects the liquid distribution along the grooves. Hence, the liquid-vapor curvature radius increases in the evaporator and adiabatic zones; however, it decreases in the condenser section. Moreover, the electric field has the same effect in the condenser section for three working fluids; however, the EHD effect is more pronounced in the evaporator zone for R123.
- ii. The liquid velocity is affected by the electric field. Indeed, the liquid velocity decreases in the evaporator and adiabatic zones. The highest liquid velocities are obtained with R123 under zero-field and EHD conditions.
- iii. The vapor velocity is affected slightly by the EHD effects whatever the working fluid. The highest vapor velocities are obtained with pentane under zero-field and EHD conditions.
- iv. The vapor pressure drop rises under the action of the electric field. However, the liquid pressure drops decreases. Furthermore, the application of the electric field diminishes the capillary pumping required for the liquid flow.
- v. R141b allows the highest heat transport capacity under the lowest optimum fill charges in zero-field and EHD conditions

- vi. Best heat transport capacities are obtained for large and deep grooves whatever the working fluid.

## References

- [1] Mansouri, J., S. Maalej, M. B. H. Sassi, and M. C. Zaghoudi. "Experimental study on the thermal performance of enhanced flat miniature heat pipes." *International Review of Mechanical Engineering* 5, no. 1 (2011): 196-208.
- [2] Zaghoudi, M. C., C. Tantolin, and C. Samo. "Experimental investigation on the use of flat mini heat pipes for avionics electronic modules cooling." *International Review of Mechanical Engineering* 5, no. 4 (2011): 770-783.
- [3] Dunn, P.D., and Reay, D.A. *Heat Pipe*. Pergamon press, Oxford, 1976.
- [4] Saad, I., S. Maalej, and M. C. Zaghoudi. "Numerical Study on an Electrohydrodynamically Driven Axially Grooved Flat Miniature Heat Pipe." *Journal of Thermophysics and Heat Transfer* 34, no. 1 (2020): 13-25.  
<https://doi.org/10.2514/1.T5623>
- [5] Durand, Émile. *Méthodes de calcul diélectriques*. Masson, 1966.
- [6] Jones, Thomas B. "The feasibility of electrohydrodynamic heat pipes." (1971).
- [7] Jones, Thomas B., and Michael P. Perry. "Electrohydrodynamic heat pipe experiments." *Journal of applied physics* 45, no. 5 (1974): 2129-2132.  
<https://doi.org/10.1063/1.1663557>
- [8] Loehrke, R. I. "An investigation of electrohydrodynamic heat pipes." (1977).
- [9] Shkilev, V. D., and BOLOGA MK. "EFFECTS OF AN ELECTRIC FIELD ON HEAT TRANSFER CHARACTERISTICS OF A HEAT PIPE." *Applied Electrical Phenomena* 2, no. 2 (1977): 61-64.
- [10] Loehrke, R. I., and W. J. Day. "Performance characteristics of several EHD heat pipe designs." *Journal of Electrostatics* 5 (1978): 285-296.  
[https://doi.org/10.1016/0304-3886\(78\)90024-4](https://doi.org/10.1016/0304-3886(78)90024-4)
- [11] Shkilev, V. D. "Operation of an electrohydrodynamic heat pipe against gravity." *Akademiia Nauk Moldavskoi SSR, Izvestiia, Serii Fiziko-Tekhnicheskikh i Matematicheskikh Nauk* 1 (1978): 89-91.
- [12] Bologa, M. K., L. L. Vasil'Ev, and V. D. Shkilev. "Effects of electric fields on heat-pipe characteristics." *Journal of engineering physics* 36, no. 6 (1979): 748-756.  
<https://doi.org/10.1007/BF01086675>
- [13] Shkilyev, V. D., and M. K. Bologa. "Heat transfer characteristics and constructive peculiarities of heat pipes utilizing the effect of electric fields." In *Advances in Heat Pipe Technology*, pp. 663-672. Pergamon, 1982.  
<https://doi.org/10.1016/B978-0-08-027284-9.50062-0>
- [14] Kikuchi, K., T. Taketani, M. Shiraishi, and T. Yamanishi. "Large scale EHD heat pipe experiments." In *Advances in Heat Pipe Technology*, pp. 643-650. Pergamon, 1982.  
<https://doi.org/10.1016/B978-0-08-027284-9.50060-7>
- [15] Bologa, M. K., and L. M. Moldavskij. "Heat pipes regulated by electric and magnetic fields." In *6th Int. Heat Pipe Conf., May 25-29, Grenoble, France*, pp. 653-660. 1987.
- [16] Bologa, M.K. and Savin, I.K. "Electrohydrodynamic Heat Pipes." In *Proceedings of the 7th International Heat Pipe Conference*, Minsk, USSR, New York: Hemisphere, pp. 549-562, 1990.
- [17] Mazurek, Wojciech B., Anna Bryszewska, and Z. Nadolny. "The influence of electric field distribution on the dielectric heat pipe performance." In *Proceedings of the 6th International Conference on Properties and Applications of Dielectric Materials (Cat. No. 00CH36347)*, vol. 2, pp. 899-902. IEEE, 2000.
- [18] Hallinan, Kevin P., Wilber Bhagat, Balamurali Kashaboina, and A. Reza Kashani. "Electro-hydrodynamic augmentation of heat transport in micro heat pipe arrays." *ASME HEAT TRANSFER DIV PUBL HTD* 361 (1998): 165-171.
- [19] Hallinan, Kevin P., and A. R. Kashani. *Electrohydrodynamic Control of Thin Film Evaporative Heat Transfer in Micro Groove Arrays*. DAYTON UNIV OH DEPT OF MECHANICAL ENGINEERING, 1999.  
<https://doi.org/10.21236/ADA378389>
- [20] Bhagat, Wilbur W. "Electrohydrodynamic enhancement of heat transport capacity of micro heat pipe arrays." *PhDT* (1999): 478.
- [21] Yu, Zhiquan, Kevin Hallinani, Wilbur Bhagat, and Reza Kashani. "Electrohydrodynamically augmented micro heat pipes." *Journal of thermophysics and heat transfer* 16, no. 2 (2002): 180-186.  
<https://doi.org/10.2514/2.6682>
- [22] Yu, Zhiquan, Kevin P. Hallinan, and Reza A. Kashani. "Temperature control of electrohydrodynamic micro heat pipes." *Experimental thermal and fluid science* 27, no. 8 (2003): 867-875.  
[https://doi.org/10.1016/S0894-1777\(03\)00059-1](https://doi.org/10.1016/S0894-1777(03)00059-1)

- [23] Suman, Balram. "A steady state model and maximum heat transport capacity of an electrohydrodynamically augmented micro-grooved heat pipe." *International journal of heat and mass transfer* 49, no. 21-22 (2006): 3957-3967.  
<https://doi.org/10.1016/j.ijheatmasstransfer.2006.04.011>
- [24] Chang, Fun Liang, and Yew Mun Hung. "Dielectric liquid pumping flow in optimally operated micro heat pipes." *International Journal of Heat and Mass Transfer* 108 (2017): 257-270.  
<https://doi.org/10.1016/j.ijheatmasstransfer.2016.12.018>
- [25] Saad, I., S. Maalej, and M. C. Zaghdoudi. "Numerical study of the electrohydrodynamic effects on the two-phase flow within an axially grooved flat miniature heat pipe." *International Journal of Heat and Mass Transfer* 107 (2017): 244-263.  
<https://doi.org/10.1016/j.ijheatmasstransfer.2016.10.089>
- [26] Saad, I., S. Maalej, and M. C. Zaghdoudi. "Modeling of the EHD effects on hydrodynamics and heat transfer within a flat miniature heat pipe including axial capillary grooves." *Journal of Electrostatics* 85 (2017): 61-78.  
<https://doi.org/10.1016/j.elstat.2016.12.004>
- [27] Saad, I., S. Maalej, and M. C. Zaghdoudi. "Combined effects of heat input power and filling fluid charge on the thermal performance of an electrohydrodynamic axially grooved flat miniature heat pipe." *Applied Thermal Engineering* 134 (2018): 469-483.  
<https://doi.org/10.1016/j.applthermaleng.2018.01.099>
- [28] Lemmon, E. W., M. L. Huber, and M. O. McLinden. "NIST Standard Reference Database 23: Reference Fluid Thermodynamic and Transport Properties-REFPROP, Version 8.0. National Institute of Standards and Technology, Standard Reference Data Program." *Standard Reference Data Program, Gaithersburg* (2018).
- [29] Suman, Balram, and Nazish Hoda. "Effect of variations in thermophysical properties and design parameters on the performance of a V-shaped micro grooved heat pipe." *International Journal of Heat and Mass Transfer* 48, no. 10 (2005): 2090-2101.  
<https://doi.org/10.1016/j.ijheatmasstransfer.2005.01.007>